2-24-2009

Estimating Porosity with Ground-Penetrating Radar Reflection Tomography: A Controlled 3-D Experiment at the Boise Hydrogeophysical Research Site

John H. Bradford
Boise State University

William P. Clement
Boise State University

Warren Barrash
Boise State University

 DOI: 10.1029/2008WR006960

Estimating porosity with ground-penetrating radar reflection tomography: A controlled 3-D experiment at the Boise Hydrogeophysical Research Site

John H. Bradford,[1] William P. Clement,[1] and Warren Barrash[1]

Received 29 February 2008; revised 27 October 2008; accepted 21 November 2008; published 24 February 2009.

[1] To evaluate the uncertainty of water-saturated sediment velocity and porosity estimates derived from surface-based, ground-penetrating radar reflection tomography, we conducted a controlled field experiment at the Boise Hydrogeophysical Research Site (BHRS). The BHRS is an experimental well field located near Boise, Idaho. The experimental data set consisted of 3-D multioffset radar acquired on an orthogonal 20 × 30 m surface grid that encompassed a set of 13 boreholes. Experimental control included (1) 1-D vertical velocity functions determined from traveltime inversion of vertical radar profiles (VRP) and (2) neutron porosity logs. We estimated the porosity distribution in the saturated zone using both the Topp and Complex Refractive Index Method (CRIM) equations and found the CRIM estimates in better agreement with the neutron logs. We found that when averaged over the length of the borehole, surface-derived velocity measurements were within 5% of the VRP velocities and that the porosity differed from the neutron log by less than 0.05. The uncertainty, however, is scale dependent. We found that the standard deviation of differences between ground-penetrating-radar-derived and neutron-log-derived porosity values was as high as 0.06 at an averaging length of 0.25 m but decreased to less than 0.02 at length scale of 11 m. Additionally, we used the 3-D porosity distribution to identify a relatively high-porosity anomaly (i.e., local sedimentary body) within a lower-porosity unit and verified the presence of the anomaly using the neutron porosity logs. Since the reflection tomography approach requires only surface data, it can provide rapid assessment of bulk hydrologic properties, identify meter-scale anomalies of hydrologic significance, and may provide input for other higher-resolution measurement methods.

Citation: Bradford, J. H., W. P. Clement, and W. Barrash (2009), Estimating porosity with ground-penetrating radar reflection tomography: A controlled 3-D experiment at the Boise Hydrogeophysical Research Site, *Water Resour. Res.*, *45*, W00D26, doi:10.1029/2008WR006960.

1. Introduction

[2] It is now well established that ground-penetrating radar (GPR) velocity measurements are a good indicator of moisture content in sandy sediments [*Greaves et al.*, 1996; *Huisman et al.*, 2003; *van Overmeeren et al.*, 1997]. Assuming low electric conductivity and that magnetic permeability is equal to that of free space, electromagnetic (EM) wave velocity is controlled by the dielectric permittivity according to the relationship $v = \frac{c}{\sqrt{\varepsilon/\varepsilon_0}}$, where v is the EM wave velocity in the material, c is the speed of light, ε_0 is the permittivity of free space, and ε is the dielectric permittivity of the material. It follows that the correlation between water content and velocity is rooted in the large dielectric permittivity contrast between water ($\varepsilon_w/\varepsilon_0 = 81$), the soil matrix ($\varepsilon_m/\varepsilon_0 \approx 4$), and air ($\varepsilon_a/\varepsilon_0 = 1$). Because of this large contrast, radar velocity is primarily a function of water content (θ_w) when $\theta_w > 5\%$ [*Topp et al.*, 1980]. In the saturated zone, θ_w is equivalent to porosity (φ). This study focuses on saturated porosity but it is important to recognize that that the sensitivity of the radar signal is really to θ_w.

[3] While it is possible to estimate subsurface porosity from GPR velocity data, it is equally important to understand the support volume over which those measurements are reliable. In estimating porosity from GPR velocity data, there are two primary sources of error. The first is error in the velocity estimate itself, and the second arises in the petrophysical transform to estimate porosity from GPR velocity where incomplete or incorrect assumptions about the physics may lead to systematic error. In this paper we are primarily concerned with the velocity estimate, but will touch to a limited extent on the problem of the petrophysical transform.

[4] The wavefield that GPR records at the surface is the result of EM wave scattering from electric property discontinuities in the subsurface. This scattered wavefield is a distorted map of electric impedance contrasts: small-scale discontinuities produce diffraction hyperbolae and dipping horizons appear to have smaller dip angles and greater length than their true geometry. The objective of wavefield

[1]Center for Geophysical Investigation of the Shallow Subsurface, Boise State University, Boise, Idaho, USA.

0043-1397/09/2008WR006960$09.00

migration is to collapse scattered energy back to its point of origin thereby producing an accurate image of reflector positions. As long as wave amplitude reconstruction is not a primary interest (e.g., we are only measuring wavefield kinematics), and with the basic assumption that the subsurface electric properties are independent of frequency, many of the migration algorithms developed for seismic data analysis can be applied directly to GPR data without modification [*Bradford et al.*, 1996; *Bradford*, 2005, 2006; *Bradford and Loughridge*, 2003; *Fisher et al.*, 1992a, 1992b; *Pipan et al.*, 2003].

[5] It is well established that prestack depth migration (PSDM) is currently the most accurate tool available for imaging reflection data. In addition to producing a map of impedance contrasts, an integral component of PSDM processing is constructing the velocity distribution. The velocity distribution produced by this approach is not subject to the assumptions of conventional normal moveout velocity analysis such as planar flat lying reflectors and small velocity gradients [*Yilmaz*, 2001]. As a result of advances in computational hardware and software, PSDM has become a standard part of the processing flow in seismic data processing for hydrocarbon exploration (see collections of papers on migration in *Leading Edge*, *24*, 2005; *21*, 2002; *20*, 2001). Perhaps the most important benefit of PSDM is the ability to correctly image data in the presence of large lateral velocity contrasts. Despite having seen little application in shallow geophysical studies, the same advantages as are found in deeper investigations may be found in both shallow seismic and GPR applications.

[6] *Stork* [1992] presents a method of tomographic velocity estimation that operates in the PSDM domain. This method of tomography takes advantage of reflector coherence and continuity in the postmigrated domain, thereby improving the processor's ability to evaluate specific reflecting horizons, particularly in a complex subsurface setting. Reflection tomography has become the preferred method of velocity model building in seismic exploration [*Guo and Fagin*, 2002]. We suggest that with increased acquisition of multifold GPR data, PSDM and reflection tomography should similarly become standard practice for the trained GPR practitioner. *Bradford* [2006, 2008] give a more thorough review of this approach to the analysis of GPR data along with examples of its application to contaminated waste site characterization. *Bradford and Wu* [2007] use the method to directly identify a high-velocity anomaly that corresponds to a zone of hydrocarbon-contaminated groundwater.

[7] While the references noted above illustrate successful applications of the reflection tomography approach, questions remain about the uncertainty in the resulting velocity models. Therefore, we conducted a controlled field experiment to test the property models resulting from a multifold GPR survey and reflection tomography processing sequence. We acquired our data set at the Boise Hydrogeophysical Research Site (BHRS). The BHRS is uniquely suited for controlled geophysical field studies in terms of both the wealth of existing control data and the opportunity to acquire additional supporting data sets as needed. In the study that follows, we evaluate the reliability of porosity estimates derived from surface GPR velocity measurements by comparing the results to borehole GPR velocity measurements and neutron log porosity estimates. We include a comparison of two petrophysical transforms commonly used in hydrogeophysical applications, the Topp [*Topp et al.*, 1980] and Complex Refractive Index Method (CRIM) [*Wharton et al.*, 1980] equations.

2. Site Description

[8] The BHRS is an experimental well field located on a gravel bar adjacent to the Boise River 15 km from downtown Boise, Idaho [*Barrash et al.*, 1999] (Figure 1). The BHRS is just upstream from the mouth of the canyon where the Boise River leaves its high-relief headwater catchment and enters the western Snake River Plain. Deposits at this site are the youngest in a series of Pleistocene to Holocene coarse fluvial deposits that mantle a sequence of successively older and higher terraces. Core and GPR reflection surveys at the BHRS support the interpretation of coarse, unconsolidated and unaltered fluvial deposits underlain by a red clay [*Barrash and Clemo*, 2002; *Barrash and Reboulet*, 2004]. Outcrop and quarry exposures in similar deposits in the Boise area show features that also have been identified in other well-studied deposits, including massive coarse-gravel sheets; sheets with weak subhorizontal layering and with planar and trough-cross-bedded coarse-gravel facies; and sand channels, lenses, and drapes [*Heinz et al.*, 2003; *Jussel et al.*, 1994; *Klingbeil et al.*, 1999].

[9] The shallow, unconfined aquifer at the BHRS has an unsaturated thickness of 0–2 m and saturated thickness that ranges between 16 and 18 m depending on seasonal variation in river stage and local depth to the red clay.

[10] The experimental well field consists of 13 wells in the central area (~20 m in diameter) and five boundary wells ~10–35 m from the central area (Figure 1). The general design of the central area wells is two concentric rings of six wells each around a central well [*Barrash et al.*, 1999]. This design supports a wide variety of single-well, cross-well, and multiple-well hydrologic and geophysical tests for thorough three-dimensional investigation of the central area [*Barrash et al.*, 2006; *Clement et al.*, 2006; *Clement and Knoll*, 2006; *Ernst et al.*, 2007; *Irving et al.*, 2007; *Johnson et al.*, 2007; *Moret et al.*, 2006].

[11] *Barrash and Clemo* [2002] and *Barrash and Reboulet* [2004] characterized the stratigraphy at the site with five distinct units on the basis of stratigraphic position in the sediment column and differentiation by porosity and lithology (Figure 2). The major characteristics of each unit are listed in Table 1. Units 1 and 3 have similar mean porosities with relatively low variances. Units 2 and 4 have similar higher porosities with greater variance. Although Units 1–4 are not visually differentiable from core samples, it is clear that Units 1 and 3 have tighter packing and were likely produced by different depositional mechanisms than Units 2 and 4 [*Barrash and Reboulet*, 2004]. Unit 5, the youngest unit, is a coarse grained, high-porosity sand channel that eroded into Unit 4. The sand channel trends northwesterly across the well field and is roughly parallel to the river. The unit pinches out toward the northeast near well A1.

[12] The five stratigraphic units have distinct geophysical boundaries as well. Clement and Knoll [*Clement and Knoll*, 2006] showed that GPR velocities (or equivalently dielectric permittivities) measured in vertical radar profiles (VRP) at the BHRS compare well with velocities predicted using

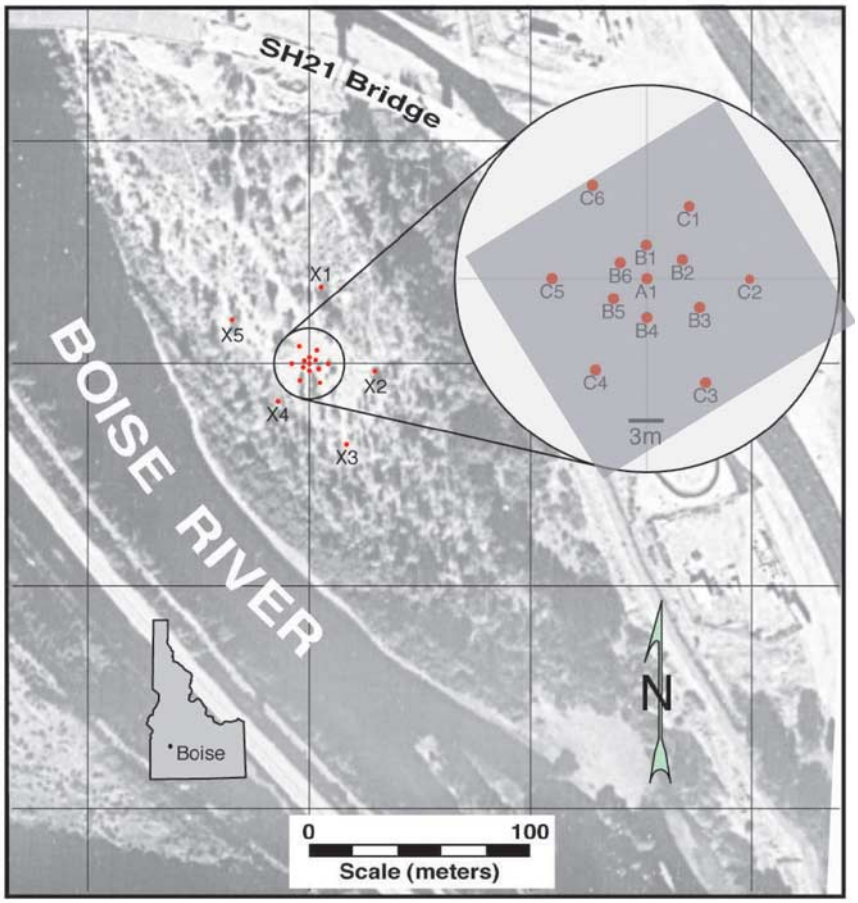

Figure 1. Location of the Boise Hydrogeophysical Research Site and the well field layout. The location of the 3-D GPR survey is shaded within the circular inset.

neutron porosity log measurements and the CRIM equation. Using 200 MHz VRP profiles, they showed that measured and predicted velocities generally fall within 95% confidence intervals at a scale of 10–20 cm indicating that the VRPs are a reliable indicator of relatively small-scale variability in porosity architecture. The velocity contrasts across the unit boundaries generate well-defined radar reflectors observed in surface GPR profiles [*Barrash and Clemo*, 2002; *Barrash and Reboulet*, 2004; *Clement et al.*, 2006], with the exception of local gradational boundary between Units 2 and 3, which does not generate a distinct GPR reflection using a 100 MHz system. Overall, however, the radar stratigraphy defines the lateral variability in position and shape of the major unit boundaries.

3. Data Acquisition and Processing

3.1. Control Data

[13] For this experiment, we used two control data sets for comparison to the surface GPR-derived property estimates (1) VRP profiles in all A, B, and C wells for velocity control and (2) porosity data derived from neutron log measurements [*Barrash and Clemo*, 2002; *Barrash and Reboulet*, 2004]. We acquired VRP data using 100 MHz antennas, a 10 cm depth sampling interval, and the center of the source antenna located 0.5 m from the well. High signal-to-noise ratios enabled reliable first arrival picking to depths up to 18 m (Figure 3). We inverted the VRP traveltime data for local 1-D velocity structure (Figure 3) using the method of Clement and Knoll [*Clement and Knoll*, 2006]. This method uses the generalized matrix to compute the model resolution and covariance matrices to estimate the standard deviation in the inverted slowness values which we use to compute velocity uncertainty. Estimated uncertainty of most VRP velocity estimates falls well within ±10%.

[14] Neutron log measurements began below the water table at a depth of approximately 2 m and extended through the full thickness of the unconfined acquifer. Logs are constructed from measurements at 0.06 m intervals but the estimated region of influence of the logging tool is a somewhat spherical volume with radius of perhaps 0.2 m [*Keys*, 1990]. The neutron logs are quite repeatable: four runs in well C5 at the BHRS have correlation coefficients in the range of 0.935–0.966 (see discussion in section 3 of *Barrash and Clemo* [2002]). Conversion of neutron counts to porosity in water-filled boreholes is well established [*Hearst and Nelson*, 1985; *Rider*, 1996] with a petrophysical transform using high and low end-member counts associated with low- and high-porosity values, respectively, for a given calibrated reservoir rock such as sandstone. No

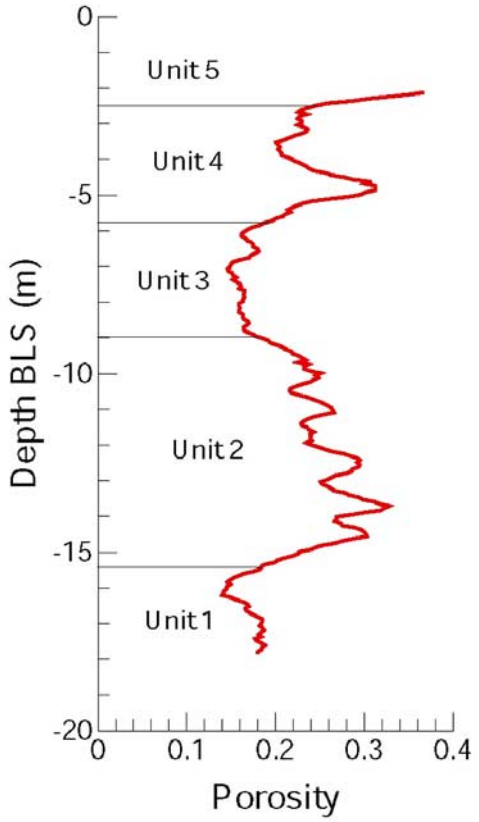

Figure 2. Representative porosity estimates derived from the neutron log with interpretation of major unit boundaries. These log-based interpretations correspond to GPR reflectivity.

similar count equivalents for porosity are available from a well at an in situ calibration site in coarse unconsolidated fluvial sediments, but end-member estimates can be made from literature values for similar deposits such as high-porosity clean fluvial sands (~0.50 [e.g., *Atkins and McBride*, 1992; *Pettyjohn et al.*, 1973]) and low-porosity conglomerate with cobble framework and sandy matrix (~0.12 [e.g., *Heinz et al.*, 2003; *Jussel et al.*, 1994]). So, working from reasonably well-constrained end-member porosity values, we estimate the uncertainty at the high end of the scale (in sand) to be ±5% and at the low end to be ±10%. Then, considering the nature of the transform and recognizing the high degree of repeatability of the logs, we can expect that rank consistency of relative porosity values is maintained to the measurement noise level (±5% accuracy

Table 1. Properties of the Five Primary Lithologic Units at the BHRS Interpreted From Cores and Neutron Porosity Logs[a]

Unit	Approximate Thickness	Mean Porosity	Porosity Variance	Dominant Composition
5	0–4 m	0.429	0.003	Coarse sand
4	1–5 m	0.232	0.002	Pebble/cobble dominated
3	3 m	0.172	0.0006	Pebble/cobble dominated
2	6 m	0.243	0.002	Pebble/cobble dominated
1	2 m	0.182	0.0006	Pebble/cobble dominated

[a]From *Barrash and Clemo* [2002].

of counts per second, see Century Geophysical Corporation website for tool specifications).

3.2. Experimental Data

3.2.1. Acquisition

[15] We acquired a 3-D, multioffset GPR data set that encompassed the A, B, and C sets of control wells (Figures 1 and 4). To acquire the multioffset data, we used the Sensors and Software Pulse EkkoPro with multichannel adapter and 100 MHz antennas. We configured the system with a single 1000 V transmitter and four receivers arranged in an in-line, off-end geometry, with antennas parallel to each other and perpendicular to the line for transverse electric (TE) polarization (Figure 5). We used an odometer wheel to trigger the system every 15 cm. For each trigger, 16 traces were vertically stacked for one receiver while the system remained in motion. With the four-receiver configuration, all receivers were sampled over every 60 cm interval. The data grid consisted of a set of orthogonal transects on 1 m centers (Figure 4). Because of surface obstructions such as well risers and trees, there were several gaps in coverage, the largest of which was a 2 m × 3 m area around well C3. The irregular coverage presented some processing challenges which we address in the data processing section below. The survey details are listed in Table 2.

[16] To acquire a broad aperture of source-receiver offsets while avoiding spatial aliasing of reflection events (critical

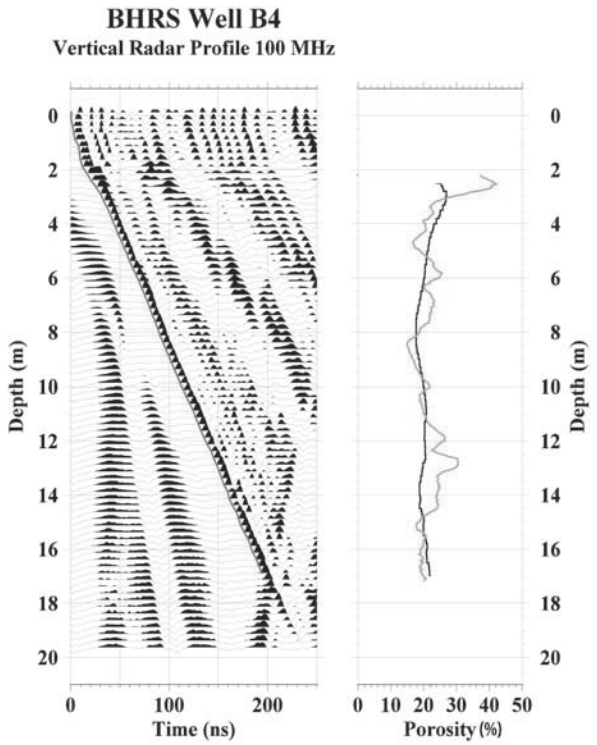

Figure 3. (left) VRP data for well B4 with first break picks shown as a solid line. (right) The porosity estimated using the inverted velocity profile with the CRIM equation (solid black line) plotted with the porosity log derived from a neutron downhole probe (solid gray line). Good signal to noise to a depth of 17 m enables reliable velocity estimation over the full aquifer thickness.

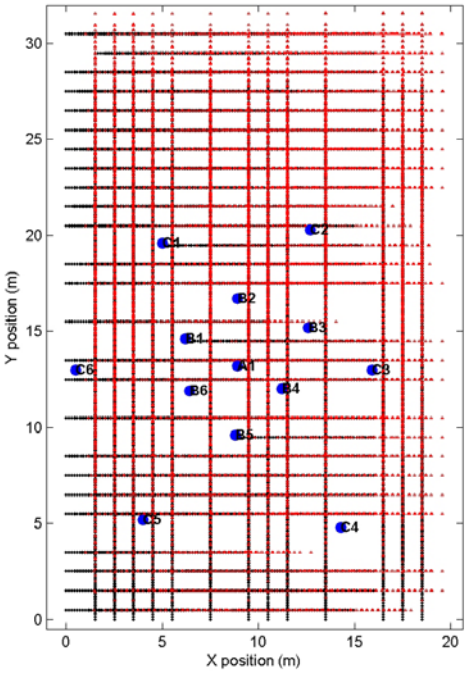

Figure 4. Source (black stars) and receiver (red triangles) geometry along with well positions. We acquired VRP profiles at all well locations to provide experimental control for the surface velocity measurements. Obstructions including well risers, trees, and bushes prevented uniform coverage of the site.

for analysis and interpretation of multioffset data), we repeated the full survey grid four times with offset ranges of 1–4, 5–8, 9–12, and 13–16 m. This geometry provided near-offset coverage to image shallow reflectors while maintaining adequate offset for velocity control at the maximum expected penetration depth of 14 m.

3.2.2. Processing

[17] The processing flow consisted of 3-D CMP binning, time zero correction, bandpass filtering (12-25-200-400 passband), 2-D PSDM and reflection tomography along in-line transects, and 3-D prestack time migration (PSTM). Below, we give details on the time zero correction, reflection tomography velocity analysis, and 3-D PSTM.

[18] The time zero correction arises since the radar system does not begin recording at the precise time that the source pulse is generated. Rather, the system begins recording prior to generation of the source pulse. This time lag ensures that all data are included within the recording time window. Many postprocessing steps and data interpretation require that the data are positioned as though the beginning of the recording, or time zero, is coincident with the generation of the source pulse. The time zero correction then consists of removing the presource recording time. With the multichannel system, the time zero correction is more complicated than that for a single-channel system. The complexity arises from the fact that fiber optic cables connecting each receiver to the control unit have slightly different lengths. These length differences produce channel-dependent timing differences. To correct for these timing differences, we first applied a linear moveout correction at air velocity in the common offset domain. We then picked the time of first motion on each trace; the first motion corresponds to the traveltime of the direct arrival through the air. The first motion traveltime of the linear moveout corrected direct air wave should correspond to time zero. We used this event to compute the traveltime correction of every individual trace. This approach also compensated for time-dependent instrument drift. With the data properly registered in time, we could then accurately measure the radar propagation velocity.

[19] For velocity analysis, we applied 2-D reflection tomography along all profiles oriented in the inline (y) direction (Figure 4). The inline direction was approximately perpendicular to the adjacent Boise River channel. We selected this orientation on the basis of previous GPR surveys which showed that the prominent Unit 4-Unit 5 stratigraphic boundary dips perpendicular to the river channel in the center of the well field. With our lines oriented parallel to this prominent dip, the 2-D velocity model assumption was reasonable as long as the cross-line velocity gradients were small. The starting model for reflection tomography was a simple 1-D model, and the same starting model was used for all profiles. We derived the velocity for the 2 m thick vadose zone from two measurements repeated for 527 CMP gathers (1) a linear fit to the direct ground arrival (the velocity is the inverse slope) and (2) a linear fit to the traveltime squared versus offset squared curve for the water table reflection in the offset range of 1–5m (the normal moveout velocity is then the square root of the inverse slope). The mean for both measurements was within one standard deviation (<3%) of 0.15 m/ns. These results indicate a constant vadose zone velocity within the resolution limits of the data, and we held the value constant at 0.15 m/ns for all tomographic inversions. The starting velocity for the saturated zone was computed by measuring the normal moveout velocity of the deepest reflector (Unit 2/Unit 1 boundary at 14 m), then using Dix inversion [*Dix*, 1955] to compute a single velocity for the saturated zone. This procedure gave a value of 0.085 m/ns for the water-saturated sands and gravels.

Figure 5. Photograph illustrating the four-receiver acquisition system. The survey was repeated four times with the near offset at 1, 5, 9, and 13 m and 1 m between receivers.

Table 2. Acquisition Parameters for the BHRS 3-D Survey

Survey Type	GPR System	Survey Size	Minimum/ Maximum Offset (m)	CMP Bin Size (m)	Source Spacing (m)	Inline Spacing (m)	Crossline Spacing (m)	Sampling Interval (ns)	Recording Time (ns)	Stacks/ Source
transverse electric,3-D, orthogonal grid	Sensors and Software PE Pro, 100 MHz unshielded antennas, 1000 V transmitter, 4 receivers, 1 transmitter	30 × 20 m (in-line × cross-line)	1/16	0.5 × 0.5	0.15	1	1	0.8	500	16

[20] After PSDM with the starting velocity model, the amount of over- or undermigration, or residual moveout, was measured along five interpreted horizons that delineate the major unit boundaries (Figure 6). Subsequent tomographic inversion optimized the velocity model to minimize the residual moveout. Finally, we applied PSDM to the data with the updated velocity model and verified that the migration result remained stable and that residual moveout was minimized. While in some cases it may be necessary to repeat this process iteratively to converge on an acceptable result, in all cases here, one round of reflection tomography produced good migration results and minimized residual moveout within the resolution limits of the data.

[21] After completing reflection tomography on all inline profiles, we interpolated the 13 2-D tomographic velocity models onto a uniform 3-D velocity grid and then applied a 3 m horizontal smoothing operator (Figure 7). From this 3-D velocity distribution we extracted vertical velocity profiles at each well position within the survey patch for detailed comparison to borehole control data.

[22] Our objectives included constructing a 3-D distribution of all major unit boundaries within the survey area. Given the irregular sampling over the survey area, we included an interpolation step in the processing stream. Further, the stratigraphic complexity at the site necessitates wavefield migration for proper positioning of the reflectors. Fortunately, it is possible to interpolate the data during migration via the migration operator. We migrated the full data set using a 3-D prestack Kirchhoff time-migration algorithm and interpolated the data onto our uniform 0.5 m × 0.5 m CMP binning grid. The migration output was a 3-D data cube in the time domain, which we

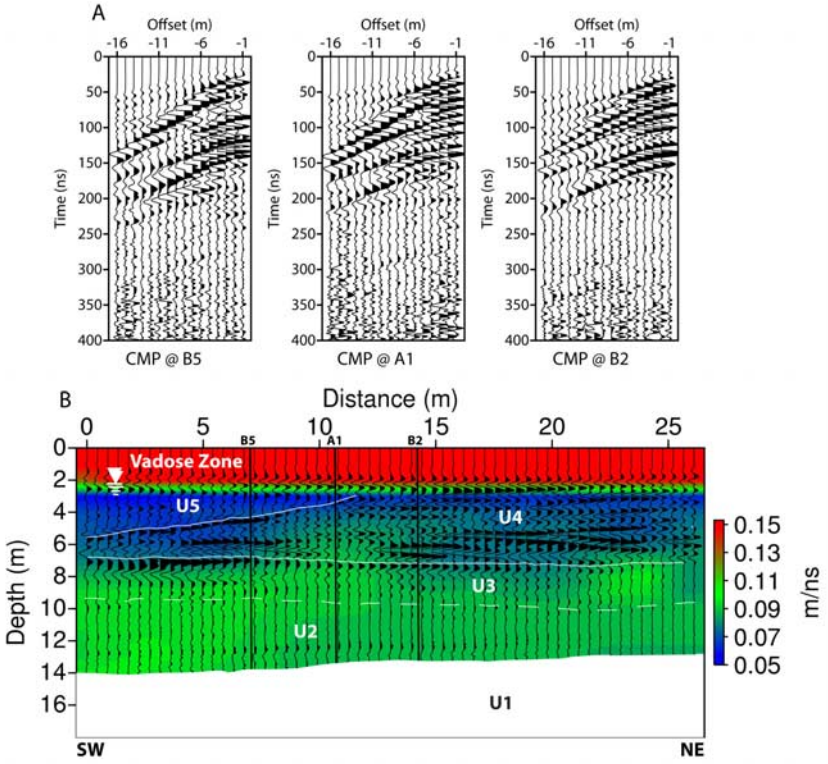

Figure 6. (a) Common midpoint gathers and (b) velocity profile through the center of the well field with the PSDM wiggle trace image overlain. Primary unit contacts are shown and correlate with the division of units interpreted from porosity log data. These units are separated by distinct reflections and velocities. The sand channel (U5) appears as a low-velocity wedge thickening toward the southwest and pinching out near A1. Note that since there are no reflectors below U1, the velocity model within U1 is unconstrained by the data.

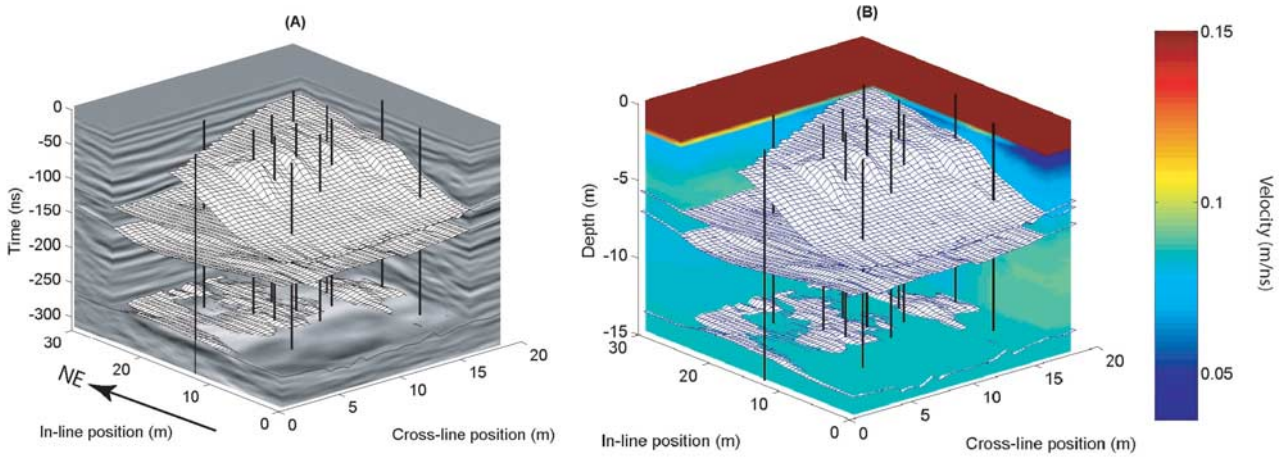

Figure 7. (a) Results of 3-D prestack time migration and interpreted boundaries of the five major lithologic units. Boreholes are shown by black lines. (b) Three-dimensional depth velocity model interpolated from 2-D reflection tomography along parallel lines oriented in the in-line direction. The topmost surface is the base of Unit 5; a sand channel that runs the full length of the site and is roughly parallel to the cross-line direction (note that the cross-line direction is parallel to flow direction of the adjacent Boise River). The deepest horizon is the top of Unit 1. The 100 MHz signal did not penetrate to the base of the aquifer at ~18 m.

converted to the depth domain using the 3-D velocity model.

4. Results

[23] Qualitatively, the results of surface data analysis compare favorably to the control VRP and porosity data (Figure 8). In all wells, the surface-data-derived velocities fall within the 95% confidence interval of the VRP-derived velocities over the majority of the borehole length. Additionally, porosity estimates derived from the surface data using the CRIM equation approximate a running average of the neutron log measured porosities.

[24] We computed the fractional difference ($\Delta v/v$) of surface-derived velocity relative to the VRP measured velocity at any particular point. The velocity difference histograms for all wells show that 89% of the surface velocity measurements fall within 10% of the VRP estimated velocities (Figure 9a). Further, the histogram shows a symmetric distribution suggesting that there is no systematic bias in the results.

[25] We took the absolute difference in porosity ($\Delta\varphi$) between surface GPR-derived values and the neutron log estimates, and computed the difference using both the Topp equation and the CRIM equation (Figures 9b and 9c). For the CRIM equation, we used a matrix relative permittivity value of 4.6, which is the value used by Clement and Knoll [*Clement and Knoll*, 2006]. Both petrophysical transforms show a bias toward underestimating the porosity. However, the CRIM equation shows somewhat better symmetry and better agreement with 63% of the porosity estimates within ±0.05 of the neutron porosity logs and 93% within 0.1. Conversely the Topp equation yields only 48% of the porosity estimates within ±0.05 of the neutron porosity logs but 91% fall within 0.1. On the basis of these results, we use the CRIM equation for all subsequent GPR-derived porosity estimates.

[26] We now consider the difference between porosity values estimated from surface GPR and from borehole-derived values averaged over a borehole length. For velocity we find that there is less than 5% difference between the means at any given borehole (Figure 10a). When averaged over all the wells, the surface-derived velocities differ from the VRP measurements by only 1.7%. A comparison of average porosities yields a similar result: the mean difference between surface GPR-derived porosities and neutron log porosities is less than 0.04 at each of the wells (Figure 10b) and when averaged over all the A, B, and C ring wells at the BHRS, the difference is 0.0041.

[27] The observations above suggest that the reliability of the surface-based measurements improve as the scale of observation increases. To better represent the scale dependence of the velocity measurements, we computed the difference between surface GPR-derived measurements and the borehole measurements as a function of vertical observation scale. In our computation, we first found the difference between the means over successively greater averaging intervals, and then computed the standard deviation of the mean differences across six different boreholes. We repeated this computation separately for the B and C groups of boreholes (Figure 11). The results for each well set are comparable. For velocity we find a maximum standard deviation of 4–6% at the smallest vertical length scale (0.25 m, the grid spacing for tomography), and then a gradual decrease to less than 2% at the maximum vertical length scale of 11 m. For the porosity estimates, the scale dependence is similar, dropping from a maximum standard deviation of 0.05–0.06 to between 0.01 and 0.02 at the 11 m vertical length scale.

5. Discussion

[28] Our results indicate that it is possible make surface-based velocity measurements that are within estimated

uncertainty of VRP-derived velocities and are comparable in vertical velocity resolution. This latter result was unexpected, particularly given that the 3-D velocity model required interpolation to fill in the irregular survey grid and extract velocity-depth functions at every borehole position. The favorable results are likely due to conducting

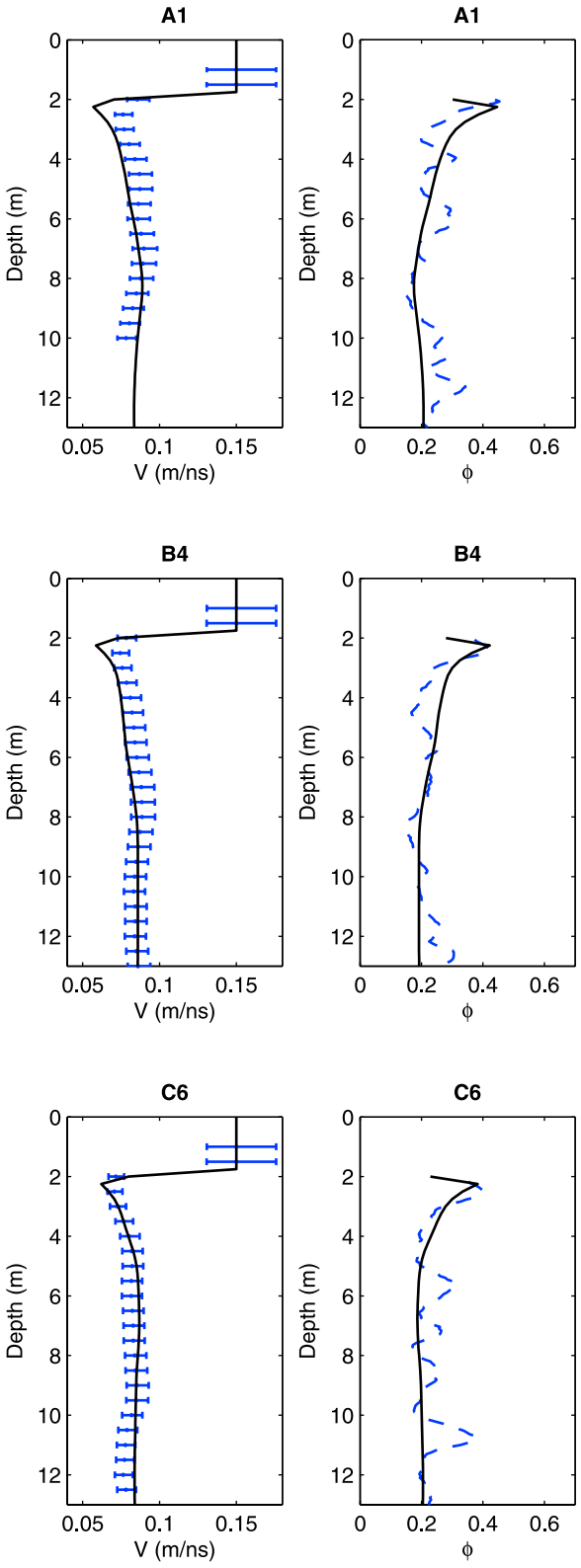

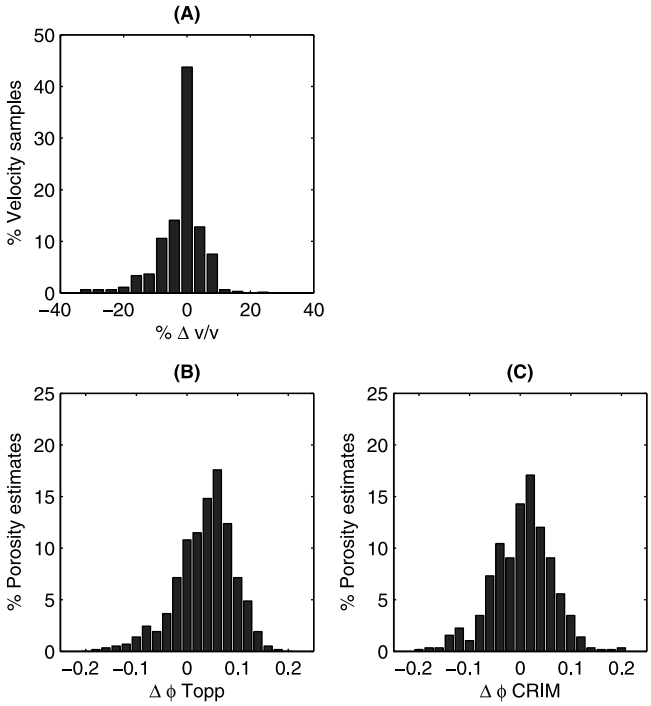

Figure 9. (a) Histogram showing the percentage of samples with a specified velocity deviation from the VRP control. Eighty-nine percent of the surface-measured velocities are within ±10% of the VRP control. Water-saturated porosity estimates from the surface velocity measurements from (b) the Topp equation and (c) the CRIM equation. The CRIM equation shows a more symmetric distribution although there is still a bias toward underestimating porosity. At the BHRS, the CRIM equation provides substantially better agreement with neutron probe porosities.

velocity analysis along lines oriented orthogonal to the primary velocity structures. At sites where primary structures are not known beforehand it may be beneficial to acquire a sparse 2-D data set for survey planning prior to full 3-D multifold acquisition. Substantial 3-D velocity heterogeneity will require full 3-D velocity inversion.

[29] We also found good agreement between GPR-derived porosity estimates and neutron porosity logs. The site-averaged porosity difference between the GPR-derived estimates and the neutron log estimates is just 0.0041. This agreement is quite remarkable, however, there is substantial scatter in the data with only 68% of the surface measure-

Figure 8. Comparison of (left) velocity and (right) porosity derived from surface GPR measurements and borehole control measurements at three wells located in the center (A), second (B), and third (C) rings of the well field. Black solid lines are from the surface GPR estimates, dots with error bars are from the VRP measurements, and dashed lines are the neutron log estimates. The surface velocity model is within the 95% confidence interval of the VRP velocities at 89% of the measurement points. The porosity estimates approximate a running average of neutron probe porosities but fail to capture the small-scale variability.

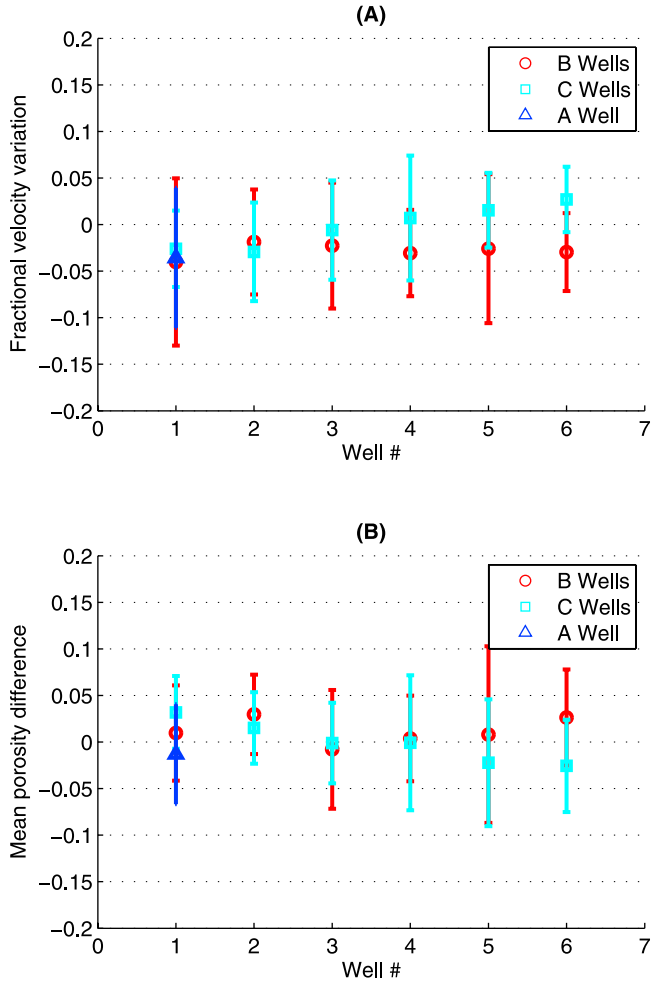

Figure 10. (a) The fractional velocity variation ($\Delta v/v$) and (b) the mean porosity difference ($\Delta\phi$) between control data and surface GPR-derived estimates. The data are averaged over the full well length and the averages are shown for all A, B, and C wells.

ments falling within ±0.05 of the neutron log measurements. A second point is that the surface GPR-derived estimates are biased toward underestimating the porosities, the maximum in the difference histogram for the CRIM equation (Figure 9c) occurs at an underestimate of 0.03. *Clement and Barrash* [2006] observed similar bias in cross-well GPR tomography results. The bias likely occurs because the electromagnetic wave velocity is more sensitive to the high-velocity material. The high-velocity material corresponds to lower water content or lower porosity. In a heterogeneous system such as is found at the BHRS, we expect a bias toward low-porosity estimates.

[30] Combining all of the above results, we make the general observation that, when averaged vertically and laterally over about 5 m, surface-derived 100 MHz GPR estimates agree with neutron log porosity measurements with a mean difference of less than 8% (absolute difference of about 0.02 from a mean porosity of 0.25). While not addressed directly in this study, we expect that the averaging length required to achieve this level of agreement is a complicated function of (1) radar wavelength and distribution of radar reflectors which control velocity resolution and (2) the porosity heterogeneity. At the BHRS, we can interpret structures in the surface GPR-derived porosity structure with confidence when averaged over 4–5 m (Figures 10 and 11).

[31] Comparing the 3-D GPR reflection image with the 3-D porosity volume, we can correlate reflector boundaries with porosity structure. The Unit 5 sand channel shows up clearly as a GPR reflection (at the base of the channel) and as a high-porosity zone (Figure 12). Further, we can identify smaller-scale features that are likely of hydrologic significance. For example, a second reflection feature, within Unit 4, appears as a linear feature oriented obliquely across the survey and corresponds to a less extensive, relatively high-porosity structure (Figure 12). It is well defined in both the reflection image and GPR-derived porosity volume.

[32] Unit 4 has been interpreted to contain relatively distinct sedimentary patches or lenses on the basis of porosity log expression and geostatistics [*Barrash and Clemo*, 2002]; the relatively high-porosity zone at about 6–7 m depth in porosity logs from wells B1-B2-C2 (Figure 12c) corresponds to the linear body evident in the radar reflection and surface GPR-derived porosity volumes. In addition, core analysis from these wells confirms the presence of

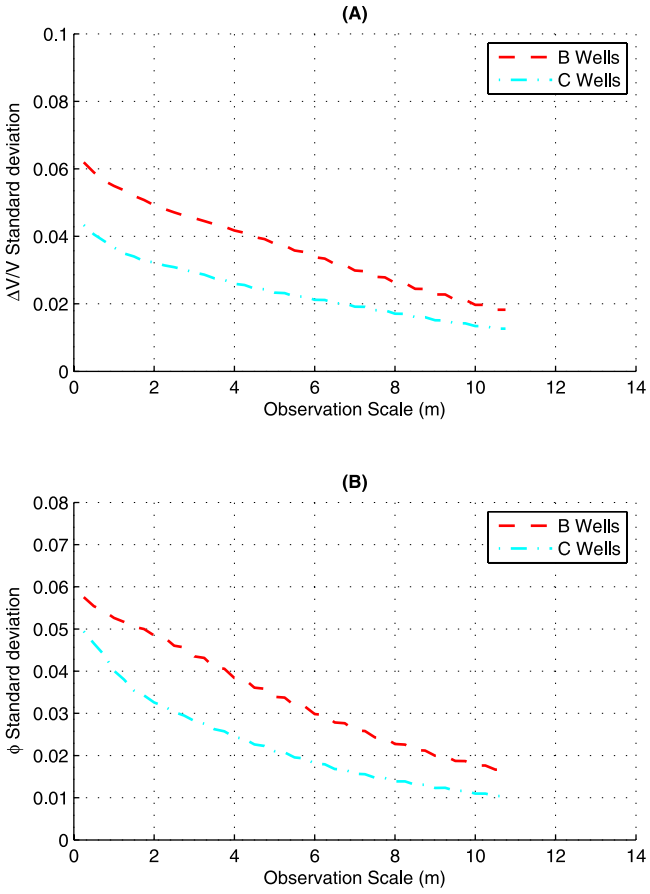

Figure 11. Standard deviation (a) in velocity and (b) in porosity as functions of observation scale. The values are taken from the mean difference between the surface GPR estimates and borehole estimates over the six boreholes that comprise a particular borehole ring. The agreement of both the velocity and porosity estimates improves substantially as a function of observation scale.

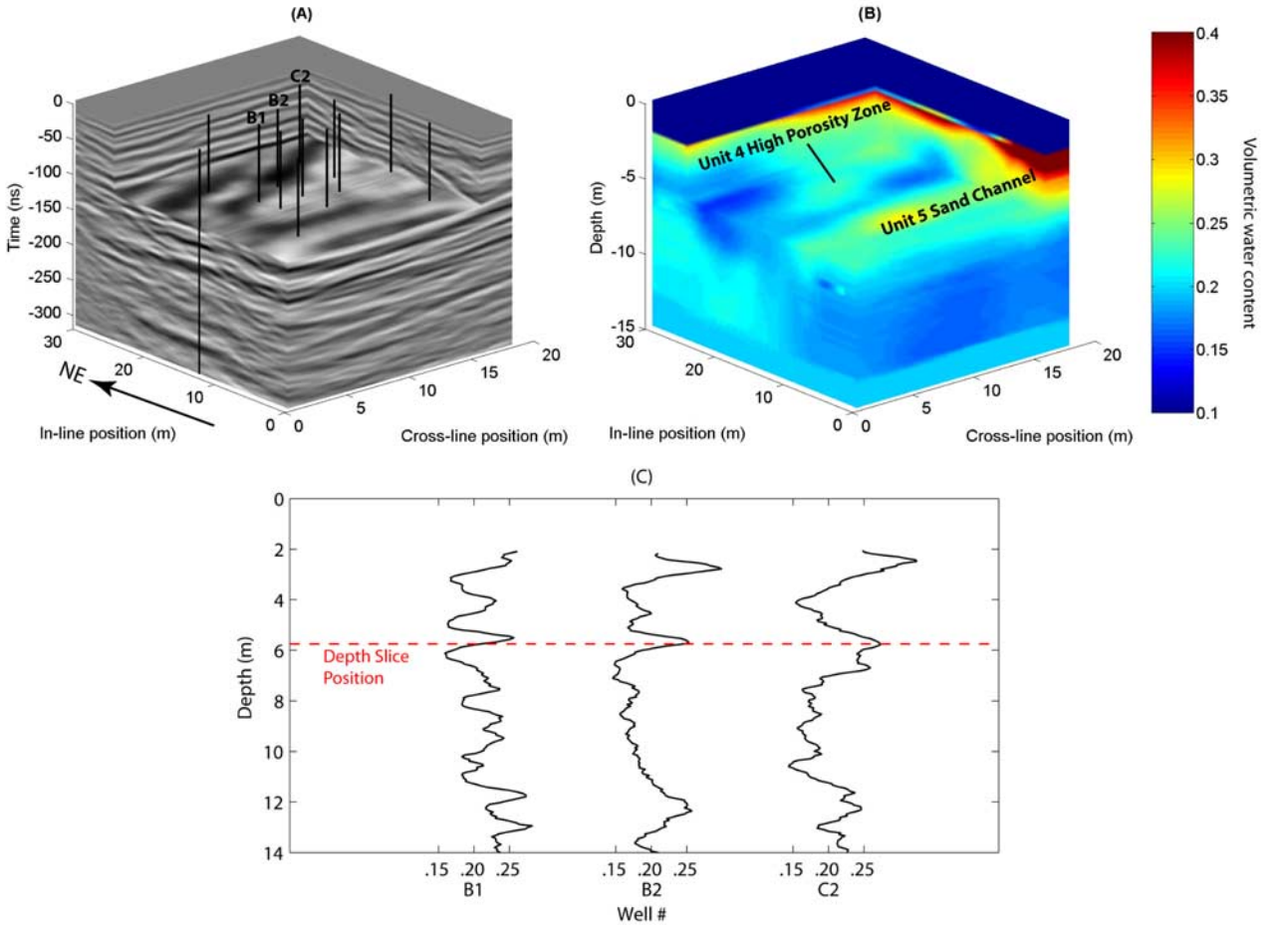

Figure 12. (a) The geometry of reflectors in the migrated GPR volume corresponds to (b) variations in the long-wavelength-saturated water content distribution. For example, the base of the Unit 5 sand channel is clearly evident in the reflection data and as a high-water-content zone. (c) Porosity logs show that the reflector that runs obliquely across the survey corresponds to a high-porosity zone (Figures 12b and 12c) and may form a preferred flow path within Unit 4.

sandier lithotypes within the 6–7 m depth range compared with core above and below [*Reboulet and Barrash*, 2003]. We have long inferred the presence of such small-scale channels or lenses from the porosity logs, but could not establish the lateral continuity of these features with a high degree of certainty from the borehole data alone because of subtle differences between nearby logs and cores.

6. Conclusions

[33] Continuous multifold GPR measurements, coupled with reflection tomography, provide a method to estimate water content in shallow aquifer systems. Below the water table these estimates correspond to aquifer porosity. The accuracy of the estimates depends on the measurement scale; at the BHRS, the 100 MHz GPR-derived porosity estimates differed from the neutron log estimates by only 0.02–0.03 when averaged over 5 m. While the spatial resolution achieved using this method may not be adequate for deterministic population of a detailed numerical flow model, the results have significant value. For example, the bulk smoothed porosity shows the trend of lateral and vertical heterogeneity at the meter scale. Additionally, the velocity or porosity information can support traditional GPR reflection interpretation. These latter two points were illustrated at the BHRS where we were able to correlate radar reflectivity with high-porosity zones that correspond to both major and minor structures within the aquifer system. As a final comment, we note that the subsurface property distributions derived through reflection tomography may prove valuable in another important application, serving as starting models for higher-resolution inverse techniques such as waveform inversion.

[34] **Acknowledgments.** The U.S. Environmental Protection Agency funded this work under grant X-97008501-0. Boise State University acknowledges support of this research by Landmark Graphics Corporation via the Landmark University Grant Program. A special acknowledgment goes to Josh Nichols, Leah Steinbronn, Joel Brown, and Dylan Mikesell for helping with the field data acquisition.

References

Atkins, J. E., and E. F. McBride (1992), Porosity and packing of Holocene river, dune, and beach sands, *AAPG Bull.*, *76*(3), 339–355.

Barrash, W., and T. Clemo (2002), Hierarchical geostatistics and multifacies systems: Boise Hydrogeophysical Research Site, Boise, Idaho, *Water Resour. Res.*, *38*(10), 1196, doi:10.1029/2002WR001436.

Barrash, W., and E. C. Reboulet (2004), Significance of porosity for stratigraphy and textural composition in subsurface coarse fluvial deposits,

Boise Hydrogeophysical Research Site, *Geol. Soc. Am. Bull.*, *116*(9/10), 1059–1073, doi:10.1130/B25370.1.

Barrash, W., T. Clemo, and M. D. Knoll (1999), Boise Hydrogeophysical Research Site (BHRS): Objectives, design, initial geostatistical results, paper presented at Symposium on the Application of Geophysics to Environmental and Engineering Problems 1999, Environ. and Eng. Geophys. Soc., Oakland, Calif.

Barrash, W., T. Clemo, J. J. Fox, and T. C. Johnson (2006), Field, laboratory, and modeling investigation of the skin effect at wells with slotted casing, Boise Hydrogeophysical Research Site, *J. Hydrol. Amsterdam*, *326*(1–4), 181–198, doi:10.1016/j.jhydrol.2005.10.029.

Bradford, J. H. (2005), Measuring lateral and vertical electromagnetic velocity in the vadose zone using GPR reflection tomography, paper presented at 75th International Meeting of the Society of Exploration Geophysicists, Soc. of Explor. Geophys., Houston, Tex.

Bradford, J. H. (2006), Applying reflection tomography in the post-migration domain to multi-fold GPR data, *Geophysics*, *71*(1), K1–K8, doi:10.1190/1.2159051.

Bradford, J. H. (2008), Measuring lateral and vertical heterogeneity in vadose zone water content using multi-fold GPR with reflection tomography, *Vadose Zone J.*, *7*, 184–193, doi:10.2136/vzj2006.0160.

Bradford, J. H., and J. Loughridge (2003), Application of two-pass migration to 3-D GPR data, paper presented at Symposium on the Application of Geophysics to Environmental and Engineering Problems 2003, Environ. and Eng. Geophys. Soc., San Antonio, Tex.

Bradford, J. H., and Y. Wu (2007), Instantaneous spectral analysis: Time-frequency mapping via wavelet matching with application to 3-D GPR contaminated site characterization, *Leading Edge*, *26*, 1018–1023, doi:10.1190/1.2769559.

Bradford, J., M. Ramaswami, and C. Peddy (1996), Imaging PVC gas pipes using 3-D GPR, paper presented at Symposium on the Application of Geophysics to Environmental and Engineering Problems 1995, Environ. and Eng. Geophys. Soc., Keystone, Colo.

Clement, W., and W. Barrash (2006), Crosshole radar tomography in a fluvial aquifer near Boise, Idaho, *J. Environ. Eng. Geophys.*, *11*, 171–184, doi:10.2113/JEEG11.3.171.

Clement, W. P., and M. D. Knoll (2006), Traveltime inversion of vertical radar profiles, *Geophysics*, *71*, K67–K76, doi:10.1190/1.2194527.

Clement, W. P., W. Barrash, and M. D. Knoll (2006), Reflectivity modeling of ground penetrating radar, *Geophysics*, *71*, K59–K66, doi:10.1190/1.2194528.

Dix, C. H. (1955), Seismic velocities from surface measurements, *Geophysics*, *34*, 180–195.

Ernst, J. R., A. G. Green, H. Maurer, and K. Holliger (2007), Application of a new 2-D time-domain full-waveform inversion scheme to crosshole radar data, *Geophysics*, *72*(5), J53–J64, doi:10.1190/1.2761848.

Fisher, E., G. A. McMechan, and A. P. Annan (1992a), Acquisition and processing of wide-aperture ground-penetrating radar data, *Geophysics*, *57*, 495–504, doi:10.1190/1.1443265.

Fisher, E., G. A. McMechan, A. P. Annan, and S. W. Cosway (1992b), Examples of reverse-time migration of single channel ground-penetrating radar profiles, *Geophysics*, *57*, 577–586, doi:10.1190/1.1443271.

Greaves, R. J., D. P. Lesmes, J. M. Lee, and M. N. Toksoz (1996), Velocity variation and water content estimated from multi-offset, ground-penetrating radar, *Geophysics*, *61*(3), 683–695, doi:10.1190/1.1443996.

Guo, N., and S. Fagin (2002), Becoming effective velocity-model builders and depth imagers, Part 2: The basics of velocity-model building, examples, and discussion, *Leading Edge*, *21*, 1210–1216.

Hearst, J. R., and P. H. Nelson (1985), *Well Logging for Physical Properties*, McGraw-Hill, New York.

Heinz, J., S. Kleineidam, G. Teutsch, and T. Aigner (2003), Heterogeneity patterns of Quaternary glaciofluvial gravel bodies (SW-Germany): Applications to hydrgeology, *Sediment. Geol.*, *158*, 1–23, doi:10.1016/S0037-0738(02)00239-7.

Huisman, J. A., S. S. Hubbard, J. D. Redman, and A. P. Annan (2003), Measuring soil water content with ground-penetrating radar: A review, *Vadose Zone J.*, *2*, 476–491.

Irving, J. D., M. D. Knoll, and R. J. Knight (2007), Improving crosshole radar velocity tomograms, *Geophysics*, *72*(4), J31–J41, doi:10.1190/1.2742813.

Johnson, T. C., P. S. Routh, W. Barrash, and M. D. Knoll (2007), A field comparison of Fresnel zone and ray-based GPR attenuation-difference tomography for time-lapse imaging of electrically anomalous tracer or contaminant plumes, *Geophysics*, *72*(2), G21–G29, doi:10.1190/1.2431638.

Jussel, P., F. Stauffer, and T. Dracos (1994), Transport modeling in heterogeneous aquifers: 1. Statistical description and numerical generation, *Water Resour. Res.*, *30*(6), 1803–1817, doi:10.1029/94WR00162.

Keys, W. S. (1990), *Borehole Geophysics Applied to Ground-Water Investigations*, 149 pp., U.S. Geol. Surv., Reston, Va.

Klingbeil, R., S. Kleineidam, U. Asprion, T. Aigner, and G. Teutsch (1999), Relating lithofacies to hydrofacies: Outcrop-based hydrogeological characterization of Quaternary gravel deposits, *Sediment. Geol.*, *129*, 299–310, doi:10.1016/S0037-0738(99)00067-6.

Moret, G. J. M., M. D. Knoll, W. Barrash, and W. C. Clement (2006), Investigating the stratigraphy of an alluvial aquifer using crosswell seismic traveltime tomography, *Geophysics*, *71*, B63–B73, doi:10.1190/1.2195487.

Pettyjohn, F., P. Potter, and R. Siever (1973), *Sand and Sandstone*, 618 pp., Springer-Verlag, New York.

Pipan, M., E. Forte, M. Dal Moro, M. Sugan, and I. Finetti (2003), Multifold ground-penetrating radar and resistivity to study the stratigraphy of shallow unconsolidated sediments, *Leading Edge*, *22*, 876–881.

Reboulet, E. C., and W. Barrash (2003), Core, grain-size, and porosity data from the Boise Hydrogeophysical Research Site: Center for Geophysical Investigation of the Shallow Subsurface, *Tech. Rep. BSU CGISS 03-02*, 87 pp., Boise State Univ., Boise, Idaho.

Rider, M. H. (1996), *The Geological Interpretation of Well Logs*, 280 pp., Gulf, Houston, Tex.

Stork, C. (1992), Reflection tomography in the postmigrated domain, *Geophysics*, *57*(5), 680–692, doi:10.1190/1.1443282.

Topp, G. C., J. L. Davis, and A. P. Annan (1980), Electromagnetic determination of soil water content: Measurements in coaxial transmission lines, *Water Resour. Res.*, *16*, 574–582, doi:10.1029/WR016i003p00574.

van Overmeeren, R. A., S. V. Sariowan, and J. C. Gehrels (1997), Ground penetrating radar for measuring volumetric soil water content; results of comparative measurements at two test sites, *J. Hydrol. Amsterdam*, *197*(1–4), 316–338, doi:10.1016/S0022-1694(96)03244-1.

Wharton, R. P., G. A. Hazen, R. N. Rau, and D. L. Best (1980), Electromagnetic propagation logging: Advances in technique and interpretation, paper presented at 55th Annual Fall Technical Conference and Exhibition, Soc. of Pet. Eng., Dallas, Tex.

Yilmaz, O. (2001), *Seismic Data Analysis*, 2027 pp., Soc. of Explor. Geophys., Tulsa, Okla.

W. Barrash, J. H. Bradford, and W. P. Clement, Center for Geophysical Investigation of the Shallow Subsurface, Boise State University, 1910 University Drive, Boise, ID 83725-1536, USA. (johnb@cgiss.boisestate.edu)